Research Square

Preprints are preliminary reports that have not undergone peer review.
They should not be considered conclusive, used to inform clinical practice,
or referenced by the media as validated information.

Stability control of towed two-wheeled trailers with an improved model and different contact force models

Hanna Zsofia Horvath

hanna.horvath@mm.bme.hu

Budapest University of Technology and Economics

Denes Takacs

Budapest University of Technology and Economics

Mate Antali

Széchenyi István University

Research Article

Keywords: Two-wheeled trailer, Stability control, Bifurcation analysis, Magic Formula, Brush tire model, Sigmoid functions

Posted Date: February 26th, 2026

DOI: https://doi.org/10.21203/rs.3.rs-8919311/v1

License: This work is licensed under a Creative Commons Attribution 4.0 International License.
Read Full License

Additional Declarations: No competing interests reported.

Version of Record: A version of this preprint was published at Journal of Sound and Vibration on February 5th, 2027. See the published version at https://doi.org/10.1016/j.jsv.2026.120202.

Stability control of towed two-wheeled trailers with an improved model and different contact force models

Hanna Zsofia Horvath · Denes Takacs · Mate Antali

Received: date / Accepted: date

Abstract This study investigates the nonlinear dynamics of towed two-wheeled trailers using a 4-DoF spatial mechanical model. That is, yaw, pitch, and roll motions are all taken into account. The nonlinear governing equations are derived using the Lagrange equation of the second kind. Geometrical nonlinearities and the non-smooth nature of the lateral tire forces are considered. The normal loads at the wheels are precisely calculated based on free-body diagrams, resulting in an improved trailer model. To extend the globally stable towing speed range, stability control is applied. Namely, a differential braking scheme is implemented based on the sign of the yaw rate of the trailer. A numerical bifurcation analysis is performed to investigate the large-amplitude vibrations and unsafe (bistable) zones, where stable rectilinear motion coexists with stable limit cycles. Bifurcation diagrams show that with appropriately chosen control gains, the size of the bistable region can be limited. Since the modeling of the tire-ground contact has a significant impact on the resulting vibrations, different contact force models are considered. Namely, the widely used Magic Formula and the brush tire models are implemented and investigated. Additionally, a family of analytical creep models is presented, which can capture the essential properties of tire forces and are easier to construct.

Keywords Two-wheeled trailer · Stability control · Bifurcation analysis · Magic Formula · Brush tire model · Sigmoid functions

Mathematics Subject Classification (2020) 70E50 · 70E60 · 70H03

H. Zs. Horvath
Department of Applied Mechanics, Faculty of Mechanical Engineering, Budapest University of Technology and Economics, Műegyetem rkp. 3., H-1111 Budapest, Hungary
E-mail: hanna.horvath@mm.bme.hu

D. Takacs
Department of Applied Mechanics, Faculty of Mechanical Engineering, Budapest University of Technology and Economics, Műegyetem rkp. 3., H-1111 Budapest, Hungary

M. Antali
Szechenyi Istvan University, Department of Applied Mechanics, Egyetem ter 1, H-9026, Gyor, Hungary

1 Introduction

Lateral stability and handling of vehicles are key issues for road transport and hence important research topics for engineers. Analyses of linear vehicle models, which formed the basis for vehicle design, date back to the 1950s and 1960s, respectively [53,40]. Nonlinear analysis was not well-established for some time and therefore, some of the phenomena in this research field remained unexplored. However, as a result of the development of mathematical tools and numerical methods, thorough nonlinear investigations have become possible. For example, the *shimmy motion* of steered wheels has been studied extensively for a long time [39,43,47]. Recently, new relevant results have been obtained using modern mathematical tools [4,7,9–11,25,28,36,42]. Thanks to these new approaches, the physical explanation of everyday problems has also become possible. For example, the *rocking motion* of suitcases was analyzed in [18, 23]. More important nonlinear vehicle dynamics problems related to road vehicles, such as the *wobble motion* of motorcycles and bicycles, have also been thoroughly studied in [16,33,34,37,41,44,45].

Two-wheeled trailers are often involved in road accidents since many drivers do not select an appropriate towing speed and/or payload position. The so-called

snaking and *rocking motions* of trailers are such unwanted vibrations that are often generated by some initial impulses or perturbations caused by the driver or by wind gusts or uneven roads [2,13,14,31,46,51]. In theoretical stability analyses, the pitch and the roll motions of the trailer are typically separated from lateral dynamics. This approach is commonly used and accepted in vehicle dynamics. However, some relevant phenomena may be unexplored when in-plane models are used. It is shown in [21,24], that the linearly independent pitch motion affects the sense of the Hopf bifurcation at the linear stability boundary. Thus, commonly used, simpler trailer models that neglect the pitch and/or the roll motion are not conservative with respect to safety and are of limited use. Based on semi-analytical and numerical bifurcation analyses, the spatial 4 DoF model can also explore the critical domains of rocking motion, associated with the loss of contact of tires. Therefore, this spatial model is recommended for exploring all possible, safety-relevant nonlinear vibrations of two-wheeled trailers.

In some cases, unwanted vibrations emerge after the design stage of the vehicle, although extensive field tests are always included. This issue led to the development of stability control algorithms. The car-trailer system can exhibit various types of loss of stability, which are referred to by different terms in the literature. To prevent jackknifing, rollover, and snaking (also called trailer sway), engineers have developed several control strategies in the last decades [12,20,29,31,52]. Three major control classes can be summarized according to the types of control actuation: differential braking, active steering, and active roll control. Differential braking can be achieved by braking either the towing car or the trailer, or both. The underlying mechanism is simple. If the yaw rate of the vehicle exceeds a threshold value, the differential braking system activates and brakes an individual wheel. Differential braking can be easily implemented on car-trailer combinations equipped with an anti-lock braking system since no additional actuators are needed [32,52]. In real applications, sensing, signal processing, and actuation all require time. Therefore, *time delay* is also introduced by the control. The presence of the time delay makes the dynamical systems infinite-dimensional and the mathematical models more complicated. On the other hand, the time delay can have a beneficial effect on the stability properties of the controlled system. For instance, it has been demonstrated that the time delay in the position control of an elastic robotic arm has a stabilizing effect [48]. Similar stabilizing effects have been observed in the case of a human-controlled towing of vehicles [49] and stabilization of an inverted pendulum [5,6].

In vehicle handling, tire modeling and tire-ground contact modeling have relevant effects on the resulting vibrations. Thus, this research field has been investigated extensively for many decades, and there are several tire models with different levels of complexity. In the simplest case, a single contact point is considered between the wheel and the ground [38]. For more complex tire models such as the *brush tire model* [9–11] and the *stretched string model* [43,50], a finite contact patch is considered, and the tire deformation is represented with spring elements. In the case of semi-empirical tire models, the tire force characteristics are specified semi-empirically, namely by using shape functions based on experiments with real tires. The most famous semi-empirical tire model is the so-called *Magic Formula* of Pacejka [39,40]. This model is widely used in the industry since it does not require the handling of a complex system of ordinary and partial differential equations. On the contrary, the exact modeling of the contact region requires many computational resources and is not analytically feasible. For this reason, engineers often use numerical tools with advanced dynamical tire models.

This study supplements the existing literature, particularly the results of [24] by offering the following novelties:

- the normal loads at the right and the left wheels are precisely calculated, based on free-body diagrams,
- braking forces are implemented to enhance stability,
- physically realistic Magic Formula factors are used to calculate lateral tire forces,
- the advantageous and disadvantageous effects of the time delay, introduced by the controlled braking forces, are shown,
- different contact force models are implemented, and their effects on the periodic solutions are shown.

The paper is organized as follows. Section 2 presents the spatial mechanical model of towed two-wheeled trailers, the configuration, the geometric constraints of the system and the kinematic expressions. Section 3 details the forces and the main sources of the nonlinearities. The nonlinear governing equations are derived using the Lagrange equation of the second kind in Sec. 4. In Sec. 5, the nonlinear governing equations are linearized around the rectilinear motion of the trailer. The effects of the vertical position of the center of gravity, the applied control gain and the feedback delay are shown in linear stability charts. Nonlinear vibrations are investigated in Sec. 6. Namely, we perform a numerical bifurcation analysis using continuation. The results are shown on bifurcation diagrams, that illustrate the effects of the applied control gain, feedback delay, and

contact force models. Our results are summarized in Sec. 7.

2 Geometry and kinematics

2.1 Spatial mechanical model

In this study, we use a 4 degrees-of-freedom (DoF) spatial mechanical model of two-wheeled trailers with non-rigid wheel suspensions [21,24], where all the yaw, pitch, and roll motions are considered, see Fig. 1. The trailer is moving in the (x_0, y_0, z_0) ground-fixed coordinate system. The system is separated into three bodies: the body of the trailer is modeled by a rigid body, and two massless material points represent the contact points of the right and the left wheels. The mass of the trailer is denoted by m and the mass moment of inertia tensor at the center of gravity C is $\mathbf{J}_\mathrm{C}$. The longitudinal and vertical positions of point C are given relative to the axle of the wheels by parameters a and h, respectively. The kingpin (point A) is towed with a constant towing speed v in the x_0 direction. The movement of the kingpin is fixed in the z_0 direction and not constrained in the y_0 direction. To have a relatively low degree-of-freedom model and a moderate number of parameters, we do not take into account the coupled dynamics of the towing car and the trailer. Hence, the interaction between them is modelled by the lateral stiffness k_lat and by the lateral damping c_lat.

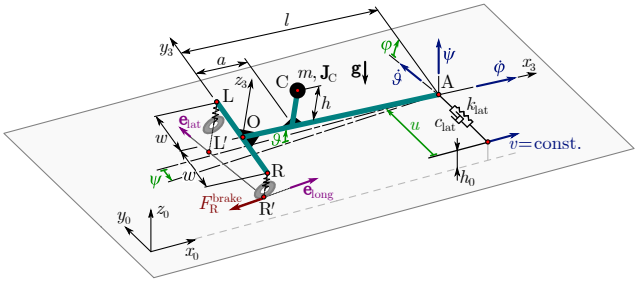


Fig. 1: The spatial, 4 DoF model of towed two-wheeled trailers together with the braking force $F_\mathrm{R}^\mathrm{brake}$ at the right wheel

The trailer is considered to be symmetric with respect to its longitudinal plane, i.e., point C is located in the center plane of the trailer. In the nominal position, the towing bar is horizontal. The constant vertical distance between the kingpin and the ground is denoted by h_0. The longitudinal distance between the axle of the massless wheels and the kingpin (i.e., the caster length) is denoted by l. The track width, i.e., the distance between the two wheels is $2w$.

For simplicity, we use a tire model that is based on the creep-force idea of [39] considering the side slip of the wheels. Then, the effect of the local deformations of the tire is applied to the rigid body model as a resultant contact force law. Accordingly, we avoid the presence of kinematic constraints, the system remains holonomic, and the equations of motion can be derived using the Lagrange equation of the second kind [19]. In addition, the resulting governing equations are ordinary differential equations, which are easier the handle.

2.2 Configuration and geometric constraints

The (possible) contact points of the wheels are located at points R' and L', see Fig. 2. These (possible) contact points are such geometrical points that define the points of action of the tire forces, and they are also used to calculate the suspension forces. In the followings, we use the term ,,possible" to include the case when the wheels leave the ground. Let us denote the distance measured between the points R and R′ with s_R, and the distance measured between points L and L′ with s_L, see Fig. 2.

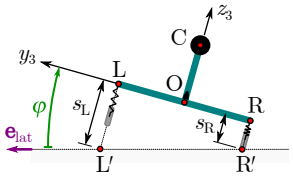


Fig. 2: The interpretations of the (possible) tire-ground contact points R′ and L′; and the distances s_R and s_L

The massless material points representing the (possible) contact points of the right and the left wheels have three DoFs each. The body of the trailer is considered as a rigid body, which has 6 DoFs. Therefore, the system has 12 DoFs altogether without constraints.

Let us investigate the geometric constraints that reduce the number of DoFs if none of the wheels separates from the ground. First, the contact points of the right and left wheels located on the ground lead to two geometric constraints. Next, the right and left suspensions constrain the motion of R′ and L′ in the longitudinal and lateral directions of the trailer, leading to overall four further geometric constraints.

Moreover, we consider that the motion of the kingpin is constrained in the longitudinal and vertical directions. The latter assumption is based on real-life observations and some related work in the literature. Videos available on trailer stability issues on highways show that vertical vibrations of the towing vehicle are

often negligible compared to lateral vibrations. Therefore, two geometric constraints can be formulated:

$$r_{\mathrm{A}}^{x_0} = vt\,, \tag{1}$$

$$r_{\mathrm{A}}^{z_0} \equiv h_0\,, \tag{2}$$

where $r_{\mathrm{A}}^{x_0}$ and $r_{\mathrm{A}}^{z_0}$ refer to the x_0 and z_0 coordinates of the kingpin A, respectively. For further details, see [21, 24].

All in all, the number of geometric constraints is 8. Thus, the system has $n = 12-8 = 4$ DoFs. To describe the configuration uniquely, one has to choose four generalized coordinates. In this study, we use the Euler angles: the yaw angle ψ, the pitch angle ϑ, the roll angle φ; and the lateral displacement of the kingpin u. Hence, the vector of generalized coordinates is

$$\mathbf{q} = \begin{bmatrix}\psi\ \vartheta\ \varphi\ u\end{bmatrix}^{\mathrm{T}}\,. \tag{3}$$

We define four frames. The ground-fixed global reference frame is denoted by $\mathcal{F}_0$ with the coordinate system (x_0, y_0, z_0). The other three reference frames $\mathcal{F}_k$ are provided by means of subsequent angular rotations: with the yaw angle ψ about the z_0-axis, with the pitch angle ϑ about the y_1-axis, and with the roll angle φ about the x_2-axis. Hence, (x_3, y_3, z_3), denoted by $\mathcal{F}_3$, is the trailer-fixed moving reference frame. The rotations, i.e., the transformation between the reference frames, can be expressed with the following transformation matrices:

$$\mathbf{T}_{0,1} = \begin{bmatrix}\cos\psi & -\sin\psi & 0\\ \sin\psi & \cos\psi & 0\\ 0 & 0 & 1\end{bmatrix}\,, \tag{4}$$

$$\mathbf{T}_{1,2} = \begin{bmatrix}\cos\vartheta & 0 & \sin\vartheta\\ 0 & 1 & 0\\ -\sin\vartheta & 0 & \cos\vartheta\end{bmatrix}\,, \tag{5}$$

$$\mathbf{T}_{2,3} = \begin{bmatrix}1 & 0 & 0\\ 0 & \cos\varphi & -\sin\varphi\\ 0 & \sin\varphi & \cos\varphi\end{bmatrix}\,. \tag{6}$$

With the help of these transformation matrices, a general expression for the transform of an arbitrary vector $\mathbf{r}$ can be derived as

$$\mathbf{r}_{\mathcal{F}_i} = \mathbf{T}_{i,j}\cdot\mathbf{r}_{\mathcal{F}_j}\,. \tag{7}$$

The transform of an arbitrary matrix $\mathbf{J}$ can be expressed as

$$\mathbf{J}_{\mathcal{F}_i} = \mathbf{T}_{i,j}\cdot\mathbf{J}_{\mathcal{F}_j}\cdot\mathbf{T}_{i,j}^{\mathrm{T}}\,, \tag{8}$$

where $\mathbf{T}_{i,j}^{\mathrm{T}}$ is the transpose of matrix $\mathbf{T}_{i,j}$. The transformation between coordinate frames n and m is a series of transformations:

$$\mathbf{T}_{n,m} = \prod_{j=n}^{m-1}\mathbf{T}_{j,j+1}\,, \tag{9}$$

where $n < m$.

When the trailer deviates from the rectilinear motion (i.e., when $\psi \neq 0$, $\vartheta \neq 0$ and $\varphi \neq 0$), the lateral and longitudinal directions with respect to the wheels do not align with x_0 and y_0. More precisely, the lateral unit vector $\mathbf{e}_{\mathrm{lat}}$ is the projection of the rotational axis of the wheels y_3 to the plane of the ground (x_0, y_0), see Figs. 1 and 2:

$$\mathbf{e}_{\mathrm{lat}} = \begin{bmatrix}\frac{\cos\psi\sin\vartheta\sin\varphi-\sin\psi\cos\varphi}{\sqrt{\sin^2\vartheta\sin^2\varphi+\cos^2\varphi}}\\ \frac{\sin\psi\sin\vartheta\sin\varphi+\cos\psi\cos\varphi}{\sqrt{\sin^2\vartheta\sin^2\varphi+\cos^2\varphi}}\\ 0\end{bmatrix}_{\mathcal{F}_0}\,. \tag{10}$$

The longitudinal direction is perpendicular to the lateral direction $\mathbf{e}_{\mathrm{lat}}$, therefore the longitudinal unit vector can be calculated in the ground-fixed reference frame as

$$\mathbf{e}_{\mathrm{long}} = \begin{bmatrix}\frac{\sin\psi\sin\vartheta\sin\varphi+\cos\psi\cos\varphi}{\sqrt{\sin^2\vartheta\sin^2\varphi+\cos^2\varphi}}\\ -\frac{\cos\psi\sin\vartheta\sin\varphi-\sin\psi\cos\varphi}{\sqrt{\sin^2\vartheta\sin^2\varphi+\cos^2\varphi}}\\ 0\end{bmatrix}_{\mathcal{F}_0}\,. \tag{11}$$

These unit vectors will be used later to express the velocity and force vectors in the corresponding directions.

2.3 Kinematics

To derive the nonlinear equations of motion using the Lagrange equation of the second kind, some kinematic quantities must be specified including the angular velocity of the trailer and the velocities of points C, A, R, L, R' and L'.

The angular velocity vector of the trailer can be represented in frame $\mathcal{F}_3$ as

$$\begin{aligned}\boldsymbol{\omega} &= \dot\psi\,\mathbf{T}_{0,3}^{-1}\begin{bmatrix}0\\0\\1\end{bmatrix}_{\mathcal{F}_0} + \dot\vartheta\,\mathbf{T}_{1,3}^{-1}\begin{bmatrix}0\\1\\0\end{bmatrix}_{\mathcal{F}_1} + \dot\varphi\,\mathbf{T}_{2,3}^{-1}\begin{bmatrix}1\\0\\0\end{bmatrix}_{\mathcal{F}_2} =\\ &= \begin{bmatrix}-\dot\psi\sin\vartheta+\dot\varphi\\ \dot\psi\cos\vartheta\sin\varphi+\dot\vartheta\cos\varphi\\ \dot\psi\cos\vartheta\cos\varphi-\dot\vartheta\sin\varphi\end{bmatrix}_{\mathcal{F}_3}\,.\end{aligned} \tag{12}$$

The velocity of the kingpin A can be calculated as the time derivative of the position vector $\mathbf{r}_{\mathrm{A}}$ in the ground-fixed $\mathcal{F}_0$ reference frame:

$$\mathbf{v}_{\mathrm{A}} = \dot{\mathbf{r}}_{\mathrm{A}} = \begin{bmatrix}v\ \dot u\ 0\end{bmatrix}_{\mathcal{F}_0}^{\mathrm{T}}\,, \tag{13}$$

where

$$\mathbf{r}_{\mathrm{A}} = \begin{bmatrix}vt\ u\ h_0\end{bmatrix}_{\mathcal{F}_0}^{\mathrm{T}} \tag{14}$$

considers the geometric constraints of Eqs. (1) and (2). The velocities of the center of gravity C and points R

and L can be expressed by means of transport formulas as

$$\mathbf{v}_{\mathrm{C}} = \mathbf{v}_{\mathrm{A}} + \boldsymbol{\omega} \times \mathbf{r}_{\mathrm{AC}} \,, \tag{15}$$

$$\mathbf{v}_{\mathrm{R}} = \mathbf{v}_{\mathrm{A}} + \boldsymbol{\omega} \times \mathbf{r}_{\mathrm{AR}} \,, \tag{16}$$

$$\mathbf{v}_{\mathrm{L}} = \mathbf{v}_{\mathrm{A}} + \boldsymbol{\omega} \times \mathbf{r}_{\mathrm{AL}} \,, \tag{17}$$

where the position vectors can be given with the geometric parameters of the trailer [21].

Based on Fig. 2, the position of point R′ can be formulated in the frame $\mathcal{F}_0$ as

$$\mathbf{r}_{\mathrm{R}'} = \mathbf{r}_{\mathrm{R}} - s_{\mathrm{R}} \, \mathbf{T}_{0,3} \left[0 \; 0 \; 1\right]^{\mathrm{T}}_{\mathcal{F}_3} \,, \tag{18}$$

where $\mathbf{r}_{\mathrm{R}} = \mathbf{r}_{\mathrm{A}} + \mathbf{r}_{\mathrm{AR}}$ and the distance s_{R} can be calculated based on the fact that R′ is the contact point of the right tire. Namely, the vertical component of its position vector is zero in the ground-fixed frame: $r^{z_0}_{\mathrm{R}'} = 0$. Knowing the position vector of Eq. (18), the velocity vector of point R′ can be calculated by differentiating with respect to time:

$$\mathbf{v}_{\mathrm{R}'} = \dot{\mathbf{r}}_{\mathrm{R}'} \,. \tag{19}$$

Similar calculations can be done for the left tire, yielding $\mathbf{r}_{\mathrm{L}'}$ and $\mathbf{v}_{\mathrm{L}'} = \dot{\mathbf{r}}_{\mathrm{L}'}$.

3 Forces and nonlinearities

Let us investigate the forces acting on the body of the trailer and the two massless material points representing the (possible) contact points of the wheels. The forces acting on the contact point of the right wheel and the body of the trailer can be seen in the free-body diagrams of Fig. 3. The classification of the external and internal, active and constraint forces is summarized in Table 1.

The overall mass m of the system is related to the body of the trailer. Therefore, the gravitational force acting on the body of the trailer can be calculated in the ground-fixed frame $\mathcal{F}_0$ as

$$\mathbf{G} = \left[0 \; 0 \; -mg\right]^{\mathrm{T}}_{\mathcal{F}_0} \,, \tag{20}$$

where g is the gravitational acceleration.

The force vector at the kingpin A contains external constraint force components in the x_0 and z_0 directions, denoted by $F^{x_0}_{\mathrm{A}}$ and $F^{z_0}_{\mathrm{A}}$. Its y_0 component takes into account the deformation of the lateral spring and damper. Thus, it is an active external force which can be calculated as

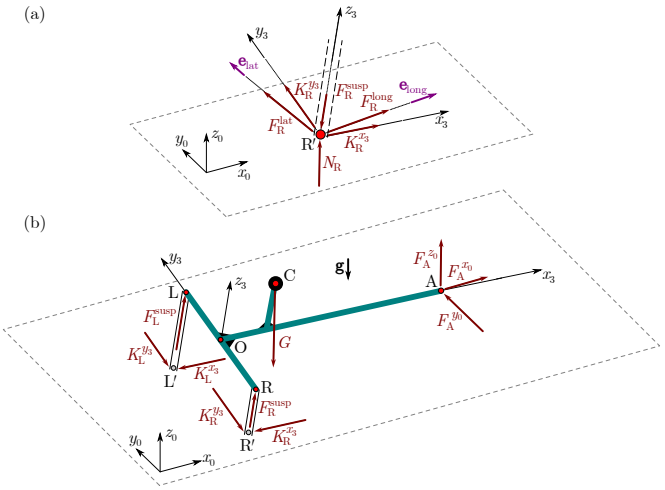


Fig. 3: Forces acting on the trailer: (a) the free-body diagram of the contact point of the right wheel represented by the massless particle at R', (b) the free-body diagram of the body of the trailer

$$F^{y_0}_{\mathrm{A}} = -k_{\mathrm{lat}} u - c_{\mathrm{lat}} \dot{u} \,. \tag{21}$$

The normal load acting on the massless particle at R' is an external constraint force from the ground. Since it is perpendicular to the ground, it only has a z_0 component, denoted by N_{R}, see Fig. 3(a). The lateral and the longitudinal components of the tire force are denoted by $F^{\mathrm{lat}}_{\mathrm{R}}$ and $F^{\mathrm{long}}_{\mathrm{R}}$, respectively. These active external forces act in the $\mathbf{e}_{\mathrm{lat}}$ lateral and the $\mathbf{e}_{\mathrm{long}}$ longitudinal directions with respect to the wheel.

The connection of the wheels to the body (i.e., the wheel suspension) is realized by the massless springs and dampers of the suspensions and by the tubes fixed to the body that constrain the wheels to move parallel to the z_3 axis. The movement of point R' is constrained by the tube in the x_3 and y_3 directions. Therefore, an internal constraint force emerges between the tube and the massless particle. The related constraint force components are denoted by $K^{x_3}_{\mathrm{R}}$ and $K^{y_3}_{\mathrm{R}}$ in the free-body diagrams.

Modeling of the suspension, lateral and longitudinal tire forces are presented in details in Subsecs. 3.1-3.3.

Table 1: Classification of the forces acting on the trailer

	Active force components	Constraint force components
External force	$G, F^{y_0}_{\mathrm{A}}, F^{\mathrm{lat}}_{\mathrm{R}}, F^{\mathrm{long}}_{\mathrm{R}}, F^{\mathrm{lat}}_{\mathrm{L}}, F^{\mathrm{long}}_{\mathrm{L}}$	$F^{x_0}_{\mathrm{A}}, F^{z_0}_{\mathrm{A}}, N_{\mathrm{R}}, N_{\mathrm{L}}$
Internal force	$F^{\mathrm{susp}}_{\mathrm{R}}, F^{\mathrm{susp}}_{\mathrm{L}}$	$K^{x_3}_{\mathrm{R}}, K^{y_3}_{\mathrm{R}}, K^{x_3}_{\mathrm{L}}, K^{y_3}_{\mathrm{L}}$

3.1 Suspension forces

Assume that the overall stiffness and the damping of the right/left tires and their suspensions are denoted by the parameters k and c, respectively. Then, the suspension force $F_{\mathrm{R}}^{\mathrm{susp}}$ originates in the deformation of the spring and the damper, and it acts as an internal active force along the z_3 direction. On the one hand, it pushes the massless particle R' to the ground, while its counterforce lifts the body of the trailer at R.

We consider that the characteristics of the wheel suspension forces are non-smooth [21,24], see Fig. 4. Namely, if the suspension is fully compressed, we consider higher stiffness and damping for the suspension. We pay special attention to the rocking motion of the trailer, namely, we consider that the right or left tire can detach from the ground, and the related normal load becomes zero. In the model, we assume that if this happens, the suspension relaxes and fully expands before the wheel touches the ground again. This assumption is based on small-scale experiments, too, see [21,24]. We neglect the effect of the unsprung mass by considering zero masses for the wheels. The suspension forces are zeros if the suspension is fully expanded. If the suspension is neither fully compressed, nor fully expanded, normal operation occurs.

Accordingly, the piece-wise smooth formula of the wheel suspension characteristics can be formulated as

$$F_{\mathrm{s}}(s,\dot{s}) = \begin{cases} F_0 + F_\infty\,, & \text{if} \quad s < L_{\min}\,, \\ F_0\,, & \text{if} \quad L_{\min} < s < L_{\max}\,, \\ 0\,, & \text{if} \quad L_{\max} < s\,, \end{cases} \tag{22}$$

for both of the right $F_{\mathrm{R}}^{\mathrm{susp}} = F_{\mathrm{s}}(s_{\mathrm{R}}, \dot{s}_{\mathrm{R}})$ and the left $F_{\mathrm{L}}^{\mathrm{susp}} = F_{\mathrm{s}}(s_{\mathrm{L}}, \dot{s}_{\mathrm{L}})$ suspension forces. In Eq. (22), the force characteristics are

$$F_0 = -k(s - L_0) - c\,\dot{s}\,, \tag{23}$$

$$F_\infty = -k_\infty(s - L_{\min}) - c_\infty\dot{s}\,, \tag{24}$$

where L_0 is the free length of the spring, $L_{\min}$ is the minimal length and $L_{\max}$ is the maximal length of the suspension. One should choose $k_\infty \gg k$ and $c_\infty \gg c$ to appropriately imitate the collision in the suspensions.

The non-smooth characteristics of Eq. (22) can also be expressed as follows:

$$F_{\mathrm{s}}(s,\dot{s}) = \mathrm{ReLU}\left(F_0 \cdot H(L_{\max} - s) + F_\infty \cdot H(L_{\min} - s)\right)\,, \tag{25}$$

where $H(x)$ is the Heaviside step-function, see e.g. [15]. The $\mathrm{ReLU}(x) = \max\{0, x\}$ function in Eq. (25) guarantees that the suspension force cannot be negative even when the suspension expands rapidly (i.e., $\dot{s} \gg 0$).

The schematic non-smooth characteristic of the suspension force $F_{\mathrm{s}}(s,0)$ for the steady-state condition $\dot{s} = 0$ together with the switchings is shown in Fig. 4.

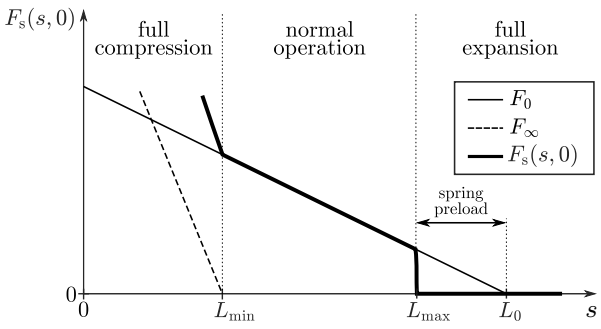


Fig. 4: The non-smooth characteristic of the suspension force $F_{\mathrm{s}}(s,0)$ for the steady-state condition $\dot{s} = 0$

3.2 Lateral tire forces

It is commonly accepted that lateral tire forces depend linearly on the normal loads [39]. Thus, the lateral tire forces are calculated as follows:

$$F_{\mathrm{R}}^{\mathrm{lat}} = -N_{\mathrm{R}}\,\mu(\alpha_{\mathrm{R}})\,, \tag{26}$$

$$F_{\mathrm{L}}^{\mathrm{lat}} = -N_{\mathrm{L}}\,\mu(\alpha_{\mathrm{L}})\,, \tag{27}$$

where $\mu(\alpha_{\mathrm{R}})$ and $\mu(\alpha_{\mathrm{L}})$ are the normalized tire force characteristics, α_{R} and α_{L} are the side slip angles of the right and left wheels, respectively.

The side slip angles for the right and the left tires can be defined by

$$\alpha_{\mathrm{R}} = \arctan\left(\frac{v_{\mathrm{R}'}^{\mathrm{lat}}}{v_{\mathrm{R}'}^{\mathrm{long}}}\right)\,, \tag{28}$$

$$\alpha_{\mathrm{L}} = \arctan\left(\frac{v_{\mathrm{L}'}^{\mathrm{lat}}}{v_{\mathrm{L}'}^{\mathrm{long}}}\right)\,, \tag{29}$$

where the lateral and longitudinal velocity components at the right and the left wheels are

$$v_{\mathrm{R}'}^{\mathrm{lat}} = \mathbf{v}_{\mathrm{R}'} \cdot \mathbf{e}_{\mathrm{lat}}\,, \quad v_{\mathrm{R}'}^{\mathrm{long}} = \mathbf{v}_{\mathrm{R}'} \cdot \mathbf{e}_{\mathrm{long}}\,, \tag{30}$$

$$v_{\mathrm{L}'}^{\mathrm{lat}} = \mathbf{v}_{\mathrm{L}'} \cdot \mathbf{e}_{\mathrm{lat}}\,, \quad v_{\mathrm{L}'}^{\mathrm{long}} = \mathbf{v}_{\mathrm{L}'} \cdot \mathbf{e}_{\mathrm{long}}\,. \tag{31}$$

Note that in Eqs. (28)-(29), we use the velocities of the (possible) contact points R' and L' to calculate the side slip angles. In many cases, the side slip angles are usually calculated using the velocity of the wheel center points. In steady-state conditions, the two different formalisms provide the same side slip angles. In transients, there are some discrepancies, which, however, may be marginal.

Throughout most of this study, the normalized tire force characteristics $\mu(\alpha_{\mathrm{R}})$ and $\mu(\alpha_{\mathrm{L}})$ are calculated using the Magic Formula [39]. The Magic Formula gives the normalized tire force characteristics as

$$\mu(\alpha_{\mathrm{R}}) = D\sin\left(C\arctan\left(B\alpha_{\mathrm{R}} - E\left(B\alpha_{\mathrm{R}} - \arctan(B\alpha_{\mathrm{R}})\right)\right)\right), \tag{32}$$

$$\mu(\alpha_{\mathrm{L}}) = D\sin\left(C\arctan\left(B\alpha_{\mathrm{L}} - E\left(B\alpha_{\mathrm{L}} - \arctan(B\alpha_{\mathrm{L}})\right)\right)\right), \tag{33}$$

where B is the stiffness factor, C is the shape factor, D is the peak factor and E is the curvature factor, see Fig. 5. These factors and their reference values are summarized in Table 2. In reality, these factors are not accurately constants but they may depend on the normal load, the temperature of the tire, the camber angle, etc., see [39]. For the sake of simplicity, we neglect these dependencies and consider fixed values in this study. Note that we also neglect the self-aligning moments of the tires, which may have a negligible effect on the final results.

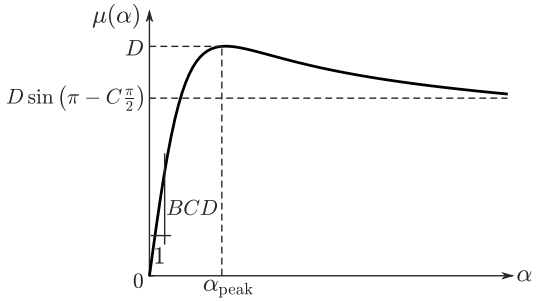


Fig. 5: The schematic characteristics of the Magic Formula [39] with constant coefficients

Table 2: The Magic Formula parameters and their reference values

Notation	Parameter name	Parameter value
B	stiffness factor	32.45
C	shape factor	1.25
D	peak factor	0.65
E	curvature factor	-1.24

3.3 Longitudinal tire forces

Although both the lateral and the longitudinal tire forces are included in our mechanical model, we do not consider any combined slip model. However, the longitudinal tire force component is calculated independently from the lateral one.

In case of an uncontrolled trailer, we assume that the longitudinal speed of the trailer is constant, rolling resistance is negligible, and no braking/driving is applied to the wheels. Consequently, the longitudinal tire forces are zeros ($F_{\mathrm{R}}^{\mathrm{long}} = 0$, $F_{\mathrm{L}}^{\mathrm{long}} = 0$).

In this study, we focus on the case of non-zero longitudinal tire forces, namely, braking is applied to enhance stability. To control the snaking motion of the trailer, we design a linear continuous-time state feedback controller, which operates with the braking forces applied to the right and the left wheels. That is, differential braking is used. For this vehicle control, we use the longitudinal forces as control inputs, without considering the longitudinal slips of the tires. Thus, by assuming negligible wheel masses, we conclude that

$$F_{\mathrm{R}}^{\mathrm{long}} = -F_{\mathrm{R}}^{\mathrm{brake}}, \tag{34}$$

$$F_{\mathrm{L}}^{\mathrm{long}} = -F_{\mathrm{L}}^{\mathrm{brake}}. \tag{35}$$

We assume that the braking forces can suddenly appear as longitudinal forces in the contact patch.

Some studies of car-trailer combinations include the yaw rate and the hitch angle (i.e., the relative yaw angle between the towing vehicle and the trailer) in the feedback control, see e.g. [12]. In [31], such control algorithms are investigated that contain the side slip angle and the yaw rate; or the hitch angle and the hitch rate; or all four of them. As a first step of the investigations, we analyze a simple control algorithm that requires measuring as few state variables as possible. Using our mechanical model, we cannot use the hitch angle or the hitch rate, since the towing car is not modeled as a vehicle. On the contrary, we assume that the yaw rate of the trailer can be measured relatively easily with an inertial measurement unit.

Consequently, we consider braking forces proportional to the yaw rate $\dot{\psi}$ with a feedback delay representing the sensor delay, the computation time, and the actuation lag altogether [21,22]. We take into account that the controller has a dead zone where no braking force is actuated. We denote the half-width of the dead zone with Ω_{dz}. Thus, the braking forces have non-smooth characteristics. A braking force is driven to the right wheel if the yaw rate exceeds Ω_{dz}, and a braking force is driven to the left wheel if the yaw rate drops below $-\Omega_{\mathrm{dz}}$. The piece-wise smooth characteristics of the right and the left braking forces $F_{\mathrm{R}}^{\mathrm{brake}}$ and $F_{\mathrm{L}}^{\mathrm{brake}}$ can be formulated as

$$F_{\mathrm{R}}^{\mathrm{brake}} = \begin{cases} K_{\mathrm{d}\psi}\left(\dot{\psi}(t-\tau) - \Omega_{\mathrm{dz}}\right), & \text{if } \dot{\psi}(t-\tau) > \Omega_{\mathrm{dz}}, \\ 0, & \text{if } \dot{\psi}(t-\tau) < \Omega_{\mathrm{dz}}, \end{cases} \tag{36}$$

$$F_{\mathrm{L}}^{\mathrm{brake}} = \begin{cases} -K_{\mathrm{d}\psi}\left(\dot{\psi}(t-\tau)+\Omega_{\mathrm{dz}}\right), & \text{if } \dot{\psi}(t-\tau) < -\Omega_{\mathrm{dz}}\,, \\ 0\,, & \text{if } \dot{\psi}(t-\tau) > -\Omega_{\mathrm{dz}}\,, \end{cases} \tag{37}$$

where $K_{\mathrm{d}\psi}$ is the control gain for the yaw rate and τ is the feedback delay. The schematic non-smooth characteristics of the braking forces can be seen in Fig. 6, both for $\Omega_{\mathrm{dz}} = 0$ and $\Omega_{\mathrm{dz}} > 0$.

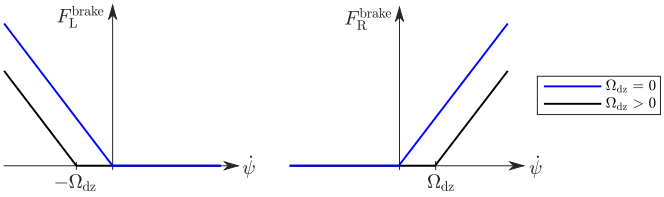


Fig. 6: The schematic non-smooth characteristics of the braking forces for $\Omega_{\mathrm{dz}} = 0$ (blue lines) and $\Omega_{\mathrm{dz}} > 0$ (black lines)

3.4 Calculation of the normal forces

In Sec. 4, we use the Lagrange equation of the second kind to derive the equations of motion. Then, the constraint forces are not provided by the derivation. However, in Eqs. (26)-(27), the expression of the normal forces are required to calculate the lateral tire forces. That is, the normal forces have to be calculated in a different way.

Let us calculate the normal force for the right wheel based on the free-body diagram of Fig. 3(a). Since the mass of the wheel is neglected, equilibrium equations can be written for the forces acting on the massless particle:

$$\mathbf{N}_{\mathrm{R}} + \mathbf{K}_{\mathrm{R}} + \mathbf{F}_{\mathrm{R}}^{\mathrm{susp}} + \mathbf{F}_{\mathrm{R}}^{\mathrm{lat}} + \mathbf{F}_{\mathrm{R}}^{\mathrm{long}} \approx \mathbf{0}\,. \tag{38}$$

Note that $\mathbf{F}_{\mathrm{R}}^{\mathrm{susp}}$ and $\mathbf{F}_{\mathrm{R}}^{\mathrm{long}}$ can be calculated based on the considerations of Subsecs. 3.1 and 3.3, while the Magic Formula $\mu(\alpha_{\mathrm{R}})$ can be substituted into $\mathbf{F}_{\mathrm{R}}^{\mathrm{lat}}$.

From the three scalar equations of the equilibrium (38), we can express the two components $K_{\mathrm{R}}^{x_3}$ and $K_{\mathrm{R}}^{y_3}$ of the constraint force, and the normal load N_{R}. Finally, we obtain

$$N_{\mathrm{R}} = \frac{f(\vartheta,\varphi)}{g(\vartheta,\varphi)}\,, \tag{39}$$

where the numerator is

$$f(\vartheta,\varphi) = F_{\mathrm{R}}^{\mathrm{susp}} \frac{1}{\cos\vartheta}\frac{1}{\cos\varphi}\sqrt{\sin^2\vartheta\sin^2\varphi+\cos^2\varphi} - \\ - F_{\mathrm{R}}^{\mathrm{long}}\tan\vartheta\frac{1}{\cos\varphi}\,, \tag{40}$$

and the denominator is

$$g(\vartheta,\varphi) = -\mu(\alpha_{\mathrm{R}})\cos\vartheta\sin\varphi + \sqrt{\sin^2\vartheta\sin^2\varphi+\cos^2\varphi}\,. \tag{41}$$

A similar free-body diagram could be drawn and similar calculations could be done for the left wheel. Based on these, the normal load at the left wheel N_{L} can be expressed with the Magic Formula $\mu(\alpha_{\mathrm{L}})$, the longitudinal $F_{\mathrm{L}}^{\mathrm{long}}$ tire force and the left wheel suspension force $F_{\mathrm{L}}^{\mathrm{susp}}$.

Note that in the model of [24], we used simplified formulations for the normal forces. This enabled us to rationalize the calculations and this model also provides similar results regarding the stability and nonlinear vibrations as the exact model investigated in this study. A comparison between the results of the approximate model of [24] and the improved (exact) model is shown in Sec. 5.

4 Nonlinear governing equations

Since the system is holonomic, the equations of motion can be derived using the Lagrange equation of the second kind [19]:

$$\frac{\mathrm{d}}{\mathrm{d}t}\frac{\partial E_{\mathrm{kin}}}{\partial \dot{q}_k} - \frac{\partial E_{\mathrm{kin}}}{\partial q_k} = Q_k, \quad k = 1,\ldots,n\,, \tag{42}$$

where E_{kin} is the kinetic energy of the system, Q_k is the k^{th} component of the generalized force, q_k is the k^{th} generalized coordinate, and $n = 4$ is the number of DoFs.

The kinetic energy of the system can be expressed as follows:

$$E_{\mathrm{kin}} = \frac{1}{2}m|\mathbf{v}_{\mathrm{C}}|^2 + \frac{1}{2}\boldsymbol{\omega}^{\mathrm{T}}\cdot\mathbf{J}_{\mathrm{C}}\cdot\boldsymbol{\omega}\,. \tag{43}$$

We assume that the axes of the (x_3, y_3, z_3) system are principal axes of inertia to simplify calculations. Therefore, the matrix of the mass moment of inertia tensor $\mathbf{J}_{\mathrm{C}}$ at the center of gravity C with respect to the trailer-fixed $\mathcal{F}_3$ reference frame is

$$\mathbf{J}_{\mathrm{C}} = \begin{bmatrix} J_{\mathrm{C}x} & 0 & 0 \\ 0 & J_{\mathrm{C}y} & 0 \\ 0 & 0 & J_{\mathrm{C}z} \end{bmatrix}_{\mathcal{F}_3}. \tag{44}$$

The mass moment of inertia of the trailer depends on the payload position. To take this into account, the following approximations are used:

$$J_{\mathrm{C}x} = m(4w^2+4h^2)/6\,, \tag{45}$$

$$J_{Cy} = m(l^2 + 4h^2)/6\,, \tag{46}$$
$$J_{Cz} = m(l^2 + 4w^2)/6\,. \tag{47}$$

Namely, J_{Cz} provides the same value as the trailer setup of [14], and J_{Cx} and J_{Cy} are formulated using the same approach.

The generalized forces of Eq. (42) can be identified as the coefficients of the virtual velocities in the virtual power of the active forces:

$$\delta P = \sum_{k=1}^{n} Q_k \delta \dot{q}_k\,. \tag{48}$$

For our system, the virtual power can be calculated by the formula

$$\begin{aligned}\delta P = {} & \mathbf{G}\cdot\delta\mathbf{v}_C + \mathbf{F}_A\cdot\delta\mathbf{v}_A + \mathbf{F}_R^{susp}\cdot\delta\mathbf{v}_R - \mathbf{F}_R^{susp}\cdot\delta\mathbf{v}_{R'} \\ & + \mathbf{F}_L^{susp}\cdot\delta\mathbf{v}_L - \mathbf{F}_L^{susp}\cdot\delta\mathbf{v}_{L'} + \mathbf{F}_R^{lat}\cdot\delta\mathbf{v}_{R'} \\ & + \mathbf{F}_L^{lat}\cdot\delta\mathbf{v}_{L'} + \mathbf{F}_R^{long}\cdot\delta\mathbf{v}_{R'} + \mathbf{F}_L^{long}\cdot\delta\mathbf{v}_{L'}\,,\end{aligned} \tag{49}$$

where $\delta\mathbf{v}_C$, $\delta\mathbf{v}_A$, $\delta\mathbf{v}_R$, $\delta\mathbf{v}_L$, $\delta\mathbf{v}_{R'}$ and $\delta\mathbf{v}_{L'}$ are the virtual velocities of points C, A, R, L, R' and L', respectively. It is trivial to calculate the virtual velocities from the velocity of each point, except for the kingpin A. For point A, the virtual velocity reads

$$\delta\mathbf{v}_A = \begin{bmatrix}0 & \delta\dot{u} & 0\end{bmatrix}^{\mathrm{T}}_{\mathcal{F}_0} \tag{50}$$

due to the rheonomic constraint of the constant towing speed v.

Considering all the nonlinearities, the nonlinear equations of motion of the controlled trailer can be written in the general form:

$$\mathbf{M}(\mathbf{q})\,\ddot{\mathbf{q}} + \mathbf{c}(\dot{\mathbf{q}}, \mathbf{q}) = \mathbf{0}\,, \tag{51}$$

where $\mathbf{M}(\mathbf{q}) \in \mathbb{R}^{4\times4}$ is the mass matrix and $\mathbf{c}(\dot{\mathbf{q}}, \mathbf{q}) \in \mathbb{R}^{4\times1}$ is a vector containing the remaining parts of the equations including all the nonlinear and non-smooth characteristics. Since we investigate the case, when the trailer is braked, $\mathbf{c}(\dot{\mathbf{q}}, \mathbf{q})$ also depends on the control gain $K_{d\psi}$ and the half-width of the dead zone Ω_{dz}. Note that thanks to the feedback delay τ, the delayed states also appear in the equations of motion, and delay differential equations describe the dynamics. Although four second-order differential equations govern the system, it has an infinite-dimensional state space. Due to the complexity of the nonlinear governing equations, no compact formula can be shown in the study.

5 Linear stability analysis

Let us investigate the case when the width of the dead zone of the controller is zero, i.e., $\Omega_{dz} = 0$. In this case, the braking forces affect the linear stability of the trailer. Thus, let us perform linear stability analysis as a first step of the investigations.

5.1 Linearized equations of motion

The nonlinear equations of motion are linearized around the steady-state $\mathbf{q}(t) \equiv \mathbf{q}_0$:

$$\begin{aligned}&\psi(t) \equiv \psi_0 = 0\,,\\ &\vartheta(t) \equiv \vartheta_0 = 0\,,\\ &\varphi(t) \equiv \varphi_0 = 0\,,\\ &u(t) \equiv u_0 = 0\,.\end{aligned} \tag{52}$$

Using the perturbation $\mathbf{y}(t) = \mathbf{q}(t) - \mathbf{q}_0$ around the rectilinear motion, the linearized equations of motion can be written as

$$\mathbf{M}_{lin}\ddot{\mathbf{y}} + \mathbf{C}_{lin}\dot{\mathbf{y}} + \mathbf{K}_{lin}\mathbf{y} = \mathbf{Q}_{lin}\,, \tag{53}$$

where $\mathbf{M}_{lin}$ is the mass matrix, $\mathbf{C}_{lin}$ is the damping matrix, $\mathbf{K}_{lin}$ is the stiffness matrix of the linearized system and $\mathbf{Q}_{lin}$ is the generalized force vector related to the control effort.

Based on $\mathbf{M}_{lin}$, $\mathbf{C}_{lin}$ and $\mathbf{K}_{lin}$, the linearized system can be separated into two subsystems [21,24]. Namely, the differential equation for the pitch motion can be disjointed and the pitch motion forms a 1 DoF subsystem with generalized coordinate ϑ, while the remaining equations are coupled (forming a 3 DoF subsystem with generalized coordinates ψ, φ and u). In vehicle dynamics, this type of separation of the vertical dynamics (pitching, bouncing) and the lateral dynamics (handling) is commonly used for linear analysis. Our mechanical model also confirms this approach for the dynamics of the trailer.

Although the 3 DoF subsystem is separated from the pitch motion, the 1 DoF subsystem is dependent on the yaw motion through the braking forces. Namely, it forms a second-order differential equation:

$$\begin{aligned}J_{Ay}\ddot{\vartheta} + 2cl^2\dot{\vartheta} + \left(2kl^2 - mgh - \frac{mgh_0(l-a)}{l}\right)\vartheta = \\ = h_0(F_R^{brake} + F_L^{brake})\,,\end{aligned} \tag{54}$$

where the mass moments of inertia about the y_3 axis at the kingpin A can be calculated as

$$J_{Ay} = J_{Cy} + m(l-a)^2 + mh^2\,. \tag{55}$$

Since the braking forces in (36) and (37) depend on the yaw rate $\dot{\psi}$, the pitch motion can be investigated based on the solution of the 3 DoF subsystem. When the 3 DoF subsystem is unstable, the pitch motion also diverges from its steady-state solution.

Therefore, let us write the governing equations for the lateral dynamics of the trailer using the perturbation vector of the 3 DoF subsystem:

$$\mathbf{y}_{\mathrm{lat}} = \begin{bmatrix} \psi & \varphi & u \end{bmatrix}^{\mathrm{T}} . \tag{56}$$

The linearized equations of motion of the 3 DoF subsystem can be written as

$$\mathbf{M}_{\mathrm{lat}}\ddot{\mathbf{y}}_{\mathrm{lat}} + \mathbf{C}_{\mathrm{lat}}\dot{\mathbf{y}}_{\mathrm{lat}} + \mathbf{K}_{\mathrm{lat}}\mathbf{y}_{\mathrm{lat}} = \mathbf{Q}_{\mathrm{lat}} , \tag{57}$$

where $\mathbf{M}_{\mathrm{lat}}$ is the mass matrix, $\mathbf{C}_{\mathrm{lat}}$ is the damping matrix and $\mathbf{K}_{\mathrm{lat}}$ is the stiffness matrix of the linearized 3 DoF subsystem:

$$\mathbf{M}_{\mathrm{lat}} = \begin{bmatrix} J_{\mathrm{A}z} & mh(l-a) & -m(l-a) \\ mh(l-a) & J_{\mathrm{A}x} & -mh \\ -m(l-a) & -mh & m \end{bmatrix} , \tag{58}$$

$$\mathbf{C}_{\mathrm{lat}} = \begin{bmatrix} 2\overline{c}l^2 & -2\overline{c}h_0 l & -2\overline{c}l \\ -2\overline{c}h_0 l & 2cw^2 + 2\overline{c}h_0^2 & 2\overline{c}h_0 \\ -2\overline{c}l & 2\overline{c}h_0 & 2\overline{c} + c_{\mathrm{lat}} \end{bmatrix} , \tag{59}$$

$$\mathbf{K}_{\mathrm{lat}} = \begin{bmatrix} 2BCD\overline{N}l & 0 & 0 \\ -2BCD\overline{N}h_0 & 2kw^2 - mgh - 2\overline{N}h_0 & 0 \\ -2BCD\overline{N} & 0 & k_{\mathrm{lat}} \end{bmatrix} . \tag{60}$$

In these matrices, the mass moments of inertia about the x_3 and the z_3 axes with respect to the kingpin A are

$$J_{\mathrm{A}x} = J_{\mathrm{C}x} + mh^2 , \tag{61}$$

$$J_{\mathrm{A}z} = J_{\mathrm{C}z} + m(l-a)^2 , \tag{62}$$

and the values of the parameters $\overline{N}$ and $\overline{c}$ are

$$\overline{N} = \frac{mg}{2}\left(1 - \frac{a}{l}\right) \quad \text{and} \quad \overline{c} = \frac{BCD}{v}\overline{N} . \tag{63}$$

The vector of generalized forces related to the control effort reads

$$\mathbf{Q}_{\mathrm{lat}} = \begin{bmatrix} -wK_{\mathrm{d}\psi}\dot{\psi}(t-\tau) & 0 & 0 \end{bmatrix}^{\mathrm{T}} . \tag{64}$$

5.2 Uncontrolled trailer

For the uncontrolled trailer, i.e., when the braking forces are zeros, the linearized equation of motion of the 1 DoF subsystem corresponding to the vertical dynamics can be written as

$$J_{\mathrm{A}y}\ddot{\vartheta} + 2cl^2\dot{\vartheta} + \left(2kl^2 - mgh - \frac{mgh_0(l-a)}{l}\right)\vartheta = 0 . \tag{65}$$

The general form of it is

$$\ddot{\vartheta} + 2\zeta\omega_{\mathrm{n}}\dot{\vartheta} + \omega_{\mathrm{n}}^2\vartheta = 0 , \tag{66}$$

where the natural angular frequency of the undamped system ω_{n} and the damping ratio ζ are defined as

$$\omega_{\mathrm{n}} = \sqrt{\frac{2kl^2 - mgh - \frac{mgh_0(l-a)}{l}}{J_{\mathrm{A}y}}} \quad \text{and} \quad \zeta = \frac{cl^2}{\omega_{\mathrm{n}}J_{\mathrm{A}y}} , \tag{67}$$

respectively. Thus, the stability criteria for the vertical dynamics correspond to

$$2kl^2 - mgh - \frac{mgh_0(l-a)}{l} > 0 \quad \text{and} \quad c > 0 . \tag{68}$$

The critical stiffness of the wheel suspension can be calculated as

$$k_{\mathrm{cr}} = mg\frac{hl + h_0(l-a)}{2l^3} . \tag{69}$$

To ensure linear stability, the stiffness of the wheel suspension must exceed the critical value k_{cr}, i.e., $k > k_{\mathrm{cr}}$ must hold. Of course, this critical stiffness is useful only during the design phase of the trailer. In the case of an existing trailer, the stability criteria of Eq. (68) may be violated by overload (i.e., $m > \frac{2kl^3}{g(hl+h_0(l-a))}$) or badly chosen position of the payload, in practice.

The linear stability of the rectilinear motion of the trailer is not affected by the pitch motion if the criteria of Eq. (68) hold. For an uncontrolled trailer, i.e., for $\mathbf{Q}_{\mathrm{lat}} = \mathbf{0}$, the linearized equations (57) and its exponential trial solution $\mathbf{y}_{\mathrm{lat}}(t) = \mathbf{A}\mathrm{e}^{\lambda t}$ with characteristic root λ, provide:

$$\left(\mathbf{M}_{\mathrm{lat}}\lambda^2 + \mathbf{C}_{\mathrm{lat}}\lambda + \mathbf{K}_{\mathrm{lat}}\right)\mathbf{A}\mathrm{e}^{\lambda t} = \mathbf{0} . \tag{70}$$

Since $\mathrm{e}^{\lambda t} > 0$ and we are not interested in the trivial solution of $\mathbf{A} = \mathbf{0}$, the following determinant (also called the characteristic function) has to be zero to fulfill Eq. (70):

$$D_{\mathrm{char}}(\lambda) := \det\left(\mathbf{M}_{\mathrm{lat}}\lambda^2 + \mathbf{C}_{\mathrm{lat}}\lambda + \mathbf{K}_{\mathrm{lat}}\right) . \tag{71}$$

The characteristic equation $D_{\mathrm{char}}(\lambda) = 0$ can be written in the form of a 6th-degree polynomial equation for the characteristic root:

$$D_{\mathrm{char}}(\lambda) = b_0\lambda^6 + b_1\lambda^5 + b_2\lambda^4 + b_3\lambda^3 + b_4\lambda^2 + b_5\lambda + b_6 = 0 . \tag{72}$$

Unfortunately, due to the complexity of the governing equations, no compact formula can be shown for the coefficients b_i of the characteristic function. The stability of the rectilinear motion can be investigated using

the Routh-Hurwitz criteria [19]. Namely, the motion is asymptotically stable if the real parts of all characteristic roots are negative: $\mathrm{Re}\lambda_i < 0$ for $\forall i$. The motion is unstable, if there exists at least one characteristic root, whose real part is positive.

On one perspective, no closed-form formula can be derived for the critical towing speed, which is a crucial parameter from vehicle stability point of view. Nevertheless, the Routh-Hurwitz criteria can be evaluated numerically for a specific set of trailer parameters. The reference values of the parameters used in this study are summarized in Table 3. These are based on the studies of [8,10,14,21].

For this reference parameter setup, dynamic stability loss occurs at $v = 29.5\,\mathrm{m/s}$. For $v > 29.5$ m/s, the real part of the rightmost complex conjugate pair of characteristic roots is positive. Consequently, the rectilinear motion is linearly unstable, and the oscillations of the trailer increase in time. For $v < 29.5$ m/s, all roots have negative real parts. Therefore, the rectilinear motion is linearly stable, and the oscillations decay in time.

Many road accidents are caused by trailers being loaded incorrectly. Therefore, it is worth investigating the effect of the payload position on the linear stability. In the linear stability chart of Fig. 7, the stability boundary is marked with a thick black curve. The gray shaded and white areas correspond to linearly stable and linearly unstable rectilinear motion, respectively. The dashed horizontal line corresponds to the reference parameter setup of Table 3. By increasing the value of the vertical position h, the critical towing speed can be considerably increased. However, the critical speed drops again for high payload positions, which is in good agreement with our physical sense.

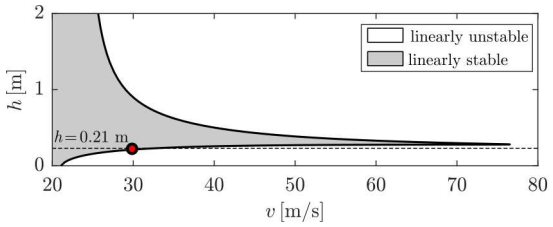


Fig. 7: Linear stability chart: the effect of the vertical position of the center of gravity on the linear stability. The dashed horizontal line corresponds to the reference parameter setup of Table 3 providing the critical towing speed 29.5 m/s marked by the red dot

The mechanical model investigated in [24] has been improved through the precise calculation of the normal loads at the right and the left wheels. The comparison between the results of the two models is shown in the linear stability charts of Fig. 8. Figure 8(a) shows the comparison for the reference parameters setup of Table 3. As can be seen, the two models basically provide the same results. However, for other parameter values, there can be a larger difference between the results of the two models, see Fig. 8(b). As can be observed, the stability boundaries are qualitatively the same, but there is a notable quantitative difference.

5.3 Controlled trailer

For the controlled trailer, the stability properties cannot be analyzed with the Routh-Hurwitz criteria anymore due to the presence of the time delay in the control loop. Hence, we use the *semi-discretization* method [26] to draw linear stability charts. The semi-discretization method approximates the infinite-dimensional monodromy

Table 3: Trailer parameters and their reference values

Notation	Parameter name	Parameter value
m	mass of the trailer	879 kg
J_{Cx}	mass moment of inertia about the x_3-axis at point C	554 kg m^2
J_{Cy}	mass moment of inertia about the y_3-axis at point C	2107 kg m^2
J_{Cz}	mass moment of inertia about the z_3-axis at point C	2601 kg m^2
a	horizontal position of point C	0.24 m
h	vertical position of point C	0.21 m
h_0	height of the kingpin	0.35 m
l	caster length	3.77 m
w	half of the track width	0.95 m
k_{lat}	lateral stiffness	13 kN/m
c_{lat}	lateral damping	0.75 kNs/m
k	stiffness of the suspension	30 kN/m
c	damping of the suspension	0.95 kNs/m
$L_{\min}$	minimal length of the spring	28 cm
$L_{\max}$	maximal length of the spring	42 cm
L_0	free length of the spring	48.5 cm

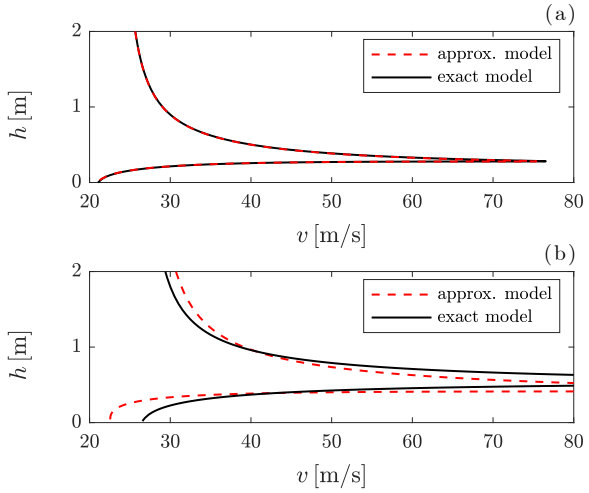


Fig. 8: Comparison between the two models: linear stability boundaries for the approximate model of [24] and the exact model. (a) For the reference parameter setup of Table 3, (b) for the reference parameter setup of Table 3, but for $k_{\mathrm{lat}} = 8.5\,\mathrm{kN/m}$, $c_{\mathrm{lat}} = 0.8\,\mathrm{kNs/m}$, $B = 18.23$, $C = 1.25$, $D = 0.65$ and $E = -1.25$

matrix of the system with a finite-dimensional one. The solution of the governing equations is asymptotically stable if all eigenvalues (characteristic multipliers) of this matrix are of modulus less than one. To perform semi-discretization, the 3 DoF subsystem is transformed into the state space form:

$$\dot{\mathbf{z}}_{\mathrm{lat}}(t) = \mathbf{A}\,\mathbf{z}_{\mathrm{lat}}(t) + \mathbf{B}\,\mathbf{u}(t-\tau)\,, \tag{73}$$

$$\mathbf{u}(t) = \mathbf{D}\,\mathbf{z}_{\mathrm{lat}}(t)\,, \tag{74}$$

where

$$\mathbf{z}_{\mathrm{lat}}(t) = \begin{bmatrix} \mathbf{y}_{\mathrm{lat}} \\ \dot{\mathbf{y}}_{\mathrm{lat}} \end{bmatrix} \tag{75}$$

and

$$\mathbf{u}(t) = [F^{\mathrm{brake}}]\,, \tag{76}$$

where

$$F^{\mathrm{brake}} = -K_{\mathrm{d}\psi}\dot{\psi}(t-\tau)\,. \tag{77}$$

Matrix $\mathbf{A}$ and vector $\mathbf{B}$ of Eq. (73) can be obtained by rearranging Eq. (57) as

$$\ddot{\mathbf{y}}_{\mathrm{lat}} = -\mathbf{M}_{\mathrm{lat}}{}^{-1}\mathbf{C}_{\mathrm{lat}}\dot{\mathbf{y}}_{\mathrm{lat}} - \mathbf{M}_{\mathrm{lat}}{}^{-1}\mathbf{K}_{\mathrm{lat}}\mathbf{y}_{\mathrm{lat}} + \mathbf{M}_{\mathrm{lat}}{}^{-1}\mathbf{Q}_{\mathrm{lat}}\,. \tag{78}$$

Thus, by collecting the coefficients, one obtains

$$\mathbf{A} = \begin{bmatrix} \mathbf{0} & \mathbf{I} \\ -\mathbf{M}_{\mathrm{lat}}{}^{-1}\mathbf{K}_{\mathrm{lat}} & -\mathbf{M}_{\mathrm{lat}}{}^{-1}\mathbf{C}_{\mathrm{lat}} \end{bmatrix}\,, \tag{79}$$

$$\mathbf{B} = \left[0\;0\;0\;\tfrac{w}{J_{\mathrm{C}z}}\;0\;\tfrac{w(l-a)}{J_{\mathrm{C}z}}\right]^{\mathrm{T}}\,, \tag{80}$$

respectively. Based on the control law of Eq. (77), the vector $\mathbf{D}$ reads

$$\mathbf{D} = \left[0\;0\;0\;-K_{\mathrm{d}\psi}\;0\;0\right]\,. \tag{81}$$

By implementing matrix $\mathbf{A}$, vectors $\mathbf{B}$ and $\mathbf{D}$ into MATLAB, one can construct the finite-dimensional approximation of the monodromy matrix [26] and draw the linear stability chart of the system in the plane of two parameters.

In the linear stability chart of Fig. 9, the stability boundary and the stable region are plotted in the plane of the towing speed v, and the control gain $K_{\mathrm{d}\psi}$. The stability chart is constructed for the reference parameter setup with a center of gravity $h = 0.27\,\mathrm{m}$ and by neglecting the time delay (i.e., $\tau = 0$). The white and the gray shaded areas correspond to linearly unstable and stable rectilinear motions, respectively. The dashed horizontal lines correspond to the uncontrolled case (i.e., $K_{\mathrm{d}\psi} = 0$). The critical towing speed, marked by the red dot, is $v = 48.6\,\mathrm{m/s}$ for this setup. Based on the linear stability chart, one can select the proper value of the control gain for an arbitrarily chosen critical towing speed.

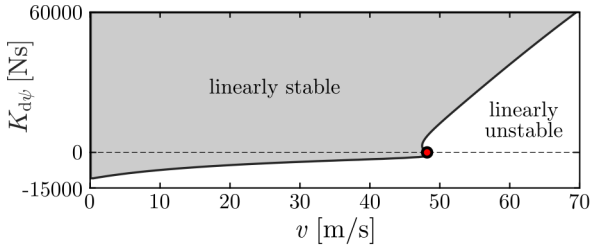


Fig. 9: Linear stability chart for the delay-free controller: the effect of the control gain on the linear stability

According to our physical sense, having a non-zero feedback delay in the control loop (i.e., $\tau > 0$) may have a significant effect on the stability properties of the trailer. Therefore, linear stability charts are shown for four different feedback delay values in Fig. 10. As can be observed in Fig. 10(a), having a small feedback delay slightly changes the stability boundaries compared to the delay-free case. The linearly stable region is remarkably larger for $\tau = 0.05\,\mathrm{s}$, see Fig. 10(b). This means that the time delay can have a beneficial effect on the stability properties.

Some former studies also explored that a time delay can have a positive effect. It was mathematically proven that for a fixed feedback gain for which the closed-loop

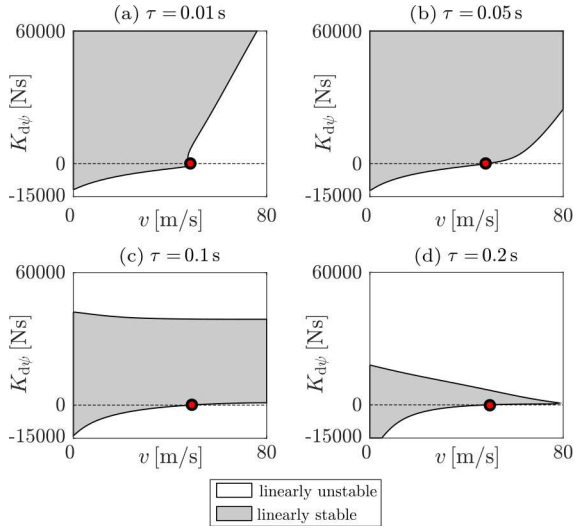


Fig. 10: Linear stability charts for different feedback delays. The dashed horizontal lines correspond to the uncontrolled case for the reference parameter setup of Table 3 with $h = 0.27\,\mathrm{m}$

system is unstable with zero delay, the non-zero time delay can ensure stability [1]. From an application point of view, a non-zero time delay can also enhance the performance of a lane-keeping controller [35].

Of course, the feedback delay cannot be arbitrarily large. Namely, for larger feedback delays, the linearly stable region shrinks considerably, see Fig. 10(c-d).

6 Nonlinear analysis

Nonlinear vibrations often significantly affect the dynamics of vehicles. For instance, the presence of unstable limit cycles in linearly stable towing speed ranges can cause large-amplitude vibrations. These limit cycles may be related to dangerous subcritical Hopf bifurcations that emerge at the linear stability boundary.

Thus, numerical bifurcation analysis is carried out with DDE-BIFTOOL [17] to obtain information about the global dynamics of the trailer. Namely, the Hopf bifurcations corresponding to the linear stability boundaries are located, and the branches of the emerging periodic solutions are followed using continuation. The originally non-smooth governing equations are approximated during the continuation by their smoothed version, using approximate Heaviside-functions, see details in [21,24]. Based on investigations on the shimmying motion of a towed rigid wheel [25], the numerical bifurcation analysis with smoothing provides reasonable results.

The detected stable and unstable limit cycles (also called periodic solutions) are depicted in bifurcation diagrams, in the plane of the towing speed v and the maximum amplitudes of the yaw angle ψ. Previous results showed that for a vertical position of the center of gravity $h = 0.27\,\mathrm{m}$, the Hopf bifurcation at the linear stability boundary is subcritical and there exists a significantly wide bistable zone. This bistable zone is considered unsafe, because the stable rectilinear motion coexist with a stable periodic solution in this towing speed region. Therefore, large enough perturbations can lead to large-amplitude vibrations. The results are shown for the reference parameter setup with $h = 0.27\,\mathrm{m}$ and considering the dead zone of the controller, i.e., $\Omega_{\mathrm{dz}} = 0.1\,\mathrm{rad/s}$.

6.1 The effect of braking

First, let us investigate the effect of the applied control gain. The results are shown for the delay-free case (i.e., $\tau = 0$). In the bifurcation diagrams of Fig. 11, the dashed and the solid curves refer to unstable and stable periodic solutions, respectively. Since the dead zone of the controller is non-zero, the critical towing speed is the same for all controller setups since the linear system is not influenced by the controller. The critical speed $v = 48.6\,\mathrm{m/s}$ where Hopf bifurcation takes place is plotted with a red dot in the bifurcation diagram.

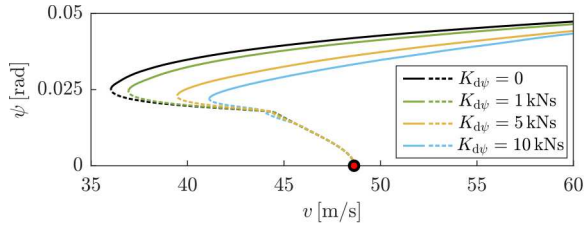


Fig. 11: Bifurcation diagrams for the yaw angle ψ with respect to the towing speed v, for the delay-free case (i.e., $\tau = 0$) and for different control gains

As can be observed in Fig. 11, the sense of the Hopf bifurcation is the same for all investigated control gain values. Namely, subcritical Hopf bifurcation takes place, and an unstable branch emerges from the Hopf point. For the uncontrolled case, the folding point of the bifurcation branch is at approx. $v = 36\,\mathrm{m/s}$, so the bistable zone is approx. 12.6 m/s wide. By increasing the value of the control gain, the width of the unsafe (bistable) zone is significantly decreased. In addition, the amplitudes of the stable periodic solutions are also decreased to some extent. Based on these results, it can be concluded that the unsafe (bistable) zone can

be reduced, and the globally stable speed range can be extended by differential braking.

6.2 The effect of feedback delay

As shown in Sec. 5, the feedback delay has a significant impact on the stability properties. Therefore, it is worth investigating its effect on the nonlinear vibrations, as well.

The effect of the feedback delay is shown in the bifurcation diagrams of Fig. 12 for a fixed control gain $K_{\mathrm{d}\psi} = 5\,\mathrm{kNs}$. As can be seen, the width of the unsafe (bistable) zone is decreased if the feedback delay is increased, e.g., for $\tau = 0.05\,\mathrm{s}$ or $\tau = 0.1\,\mathrm{s}$. The amplitudes of the corresponding periodic solutions are also considerably smaller. These are counterintuitive results since they suggest that the feedback delay is indeed beneficial. Of course, a very large feedback delay degrades the performance of the controller. For $\tau > 0.1\,\mathrm{s}$, the width of the unsafe zone is increased again. Note that for $\tau > 0.2\,\mathrm{s}$, the vibration amplitudes are also increased compared to the delay-free case.

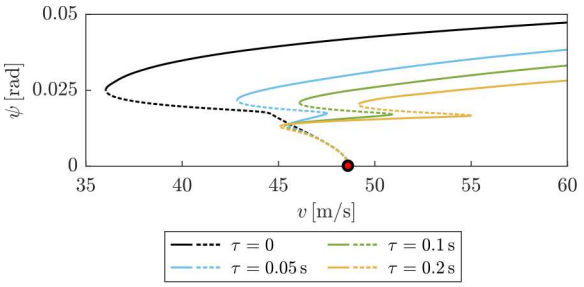


Fig. 12: Bifurcation diagrams for the yaw angle ψ with respect to the towing speed v, for a fixed control gain $K_{\mathrm{d}\psi} = 5\,\mathrm{kNs}$ and for different feedback delays

6.3 The effect of the used contact force model

Until now, the Magic Formula has been used to calculate lateral tire forces. Using the Magic Formula has its advantages and disadvantages. On the one hand, its characteristics is smooth and the lateral tire force can be calculated with a single formula for all side slip angles. In addition, it is easy to implement into any mechanical model. On the other hand, extensive experimentation is required to precisely determine its factors precisely for every type of tire, which may restrict convenient use. Moreover, it is not clear how each factor of the formula affects the characteristics. For instance, the slope of the curve at the origin depends on the product BCD and D also affects the peak value of the characteristics, see Fig. 5. Therefore, the peak factor D simultaneously affects two properties. Let us investigate different contact force models. Namely, let us use the brush tire model and a family of creep models when calculating the lateral tire forces.

6.3.1 Brush tire model

The brush tire model [39] is one of the most used physical tire models, since it is relatively simple, but still captures the dynamic tire-ground contact. The tire is assumed to be a rigid wheel-rim and the tire tread is represented by massless, elastic elements with distributed lateral stiffness and damping. These elastic elements are pressed to the ground in the contact patch, where they either stick to or slide on the ground. The longitudinal deformation of the elastic elements is not considered here. The lateral tire deformation generates a distributed force. The resultant lateral tire force can be calculated by integrating the distributed force in the whole contact patch [7,8,39].

With the brush tire model, the lateral tire force can be calculated with the static μ_0 and the dynamic μ coefficient of friction and the so-called cornering stiffness $\tilde{C}$. The brush tire model parameters and their reference values used in this study are summarized in Table 4. The cornering stiffness depends on the half-length of the contact patch and the stiffness of the elastic elements. In reality, these depend on the normal loads, too. However, we assume that the cornering stiffness is constant to simplify the calculations. To be able to match the lateral tire force characteristics with the Magic Formula, we normalize the tire force with the nominal vertical load.

Table 4: The brush tire model parameters and their reference values

Notation	Parameter name	Parameter value
μ_0	static coeff. of friction	0.9
μ	dynamic coeff. of friction	0.6
$\tilde{C}$	cornering stiffness	113000 N

The normalized tire force characteristics given by the brush tire model can be formulated as

$$\mu(\alpha) = \begin{cases} \overline{\phi}_1 \tan\alpha + \overline{\phi}_2 \tan^2\alpha \,\mathrm{sign}\alpha \\ \quad + \overline{\phi}_3 \tan^3\alpha\,, & \text{if} \quad 0 \le |\alpha| \le \alpha_{\mathrm{cr}}\,, \\ \mu\,\mathrm{sign}\alpha\,, & \text{if} \quad |\alpha| > \alpha_{\mathrm{cr}}\,, \end{cases} \tag{82}$$

where the critical side slip angle at which the sliding region expands to the whole contact patch is

$$\alpha_{\mathrm{cr}} = \arctan\left(\frac{3\mu_0 N_0}{\tilde{C}}\right) . \tag{83}$$

with the nominal vertical load $N_0 = mg/2$. In Eq. (82), the normalized coefficients of the brush tire model are

$$\overline{\phi}_1 = \overline{C} = \frac{\tilde{C}}{N_0} , \tag{84}$$

$$\overline{\phi}_2 = -\frac{\overline{C}^2}{3\mu_0}\left(2 - \frac{\mu}{\mu_0}\right) , \tag{85}$$

$$\overline{\phi}_3 = \frac{\overline{C}^3}{9\mu_0^2}\left(1 - \frac{2\mu}{3\mu_0}\right) , \tag{86}$$

respectively.

In this study, we match the Magic Formula factors with the parameters of the brush tire model. Hence, their characteristics agree in several aspects, see Fig. 13(a):

- the slope at the origin is the same,
- the maximum of the characteristics is the same,
- the maximum of the characteristics occurs at the same side slip angle α_{peak},
- for large side slip angles (i.e., $\alpha \to \infty$), both characteristics yield $\mu(\alpha) = \mu$.

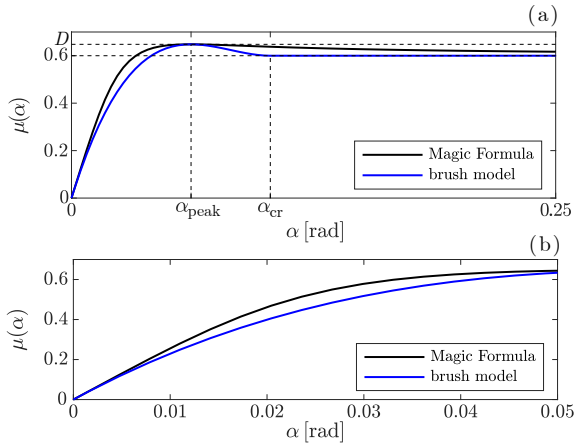


Fig. 13: The normalized tire force characteristics $\mu(\alpha)$ calculated with the Magic Formula and the brush tire model

By matching the two characteristics according to these aspects, one can observe that for small side slip angles, i.e., $0.01\,\mathrm{rad} < \alpha < 0.05\,\mathrm{rad}$, there is a notable difference between the two characteristics, see Fig. 13(b). Previous studies have shown that the side slip angle usually remains within this range. Thus, notable differences in nonlinear vibrations are suspected when using the brush tire model.

The effect of using the brush tire model is shown in the bifurcation diagrams of Fig. 14 for both the uncontrolled and controlled trailers. In the case of the Magic Formula and the brush tire model, the unstable and stable periodic solutions are shown with black and blue curves, respectively. As shown in the enlarged sections of the bifurcation diagrams, a stable limit cycle emerges from the Hopf point in a conical structure when using the brush tire model. This is due to its non-smooth nature [7]. The characteristics of the Magic Formula is smooth. Thus, the unstable limit cycles emerge in a paraboloid structure.

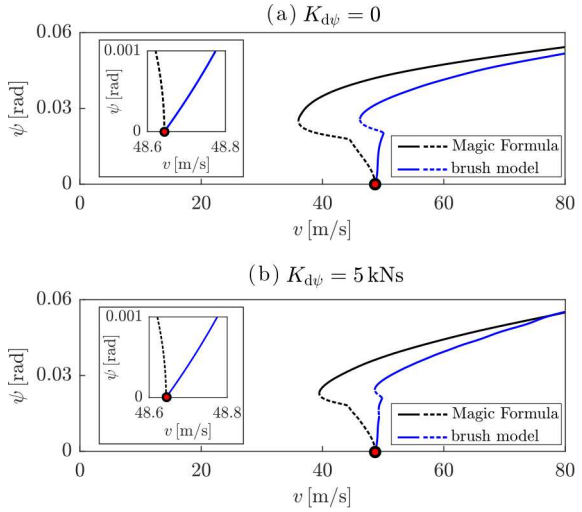


Fig. 14: Bifurcation diagrams for the yaw angle ψ with respect to the towing speed v with the Magic Formula and the brush tire model, (a) for $K_{\mathrm{d}\psi} = 0$ and (b) for $K_{\mathrm{d}\psi} = 5\,\mathrm{kNs}$

As can be observed in Fig. 14(a), the width of the unsafe (bistable) zone is relevantly decreased and the amplitudes of the vibrations are also decreased to some extent when applying the brush tire model. The width of the unsafe (bistable) zone is further decreased in case of the controlled trailer, see Fig. 14(b). However, the vibration amplitudes exceed the ones corresponding to the Magic Formula for larger towing speeds.

Based on Fig. 14, it can be concluded that the structure and nature of the emerging limit cycles and vibration amplitudes differ significantly when the Magic Formula and brush tire model are implemented. Therefore, this study emphasizes the importance of selecting the appropriate contact force model for our system. Further theoretical and experimental investigation is needed to determine which model is closer to reality. In addition, it is suspected that the difference in results would be smaller if the normalized tire force charac-

teristics matched more closely at small side slip angles. Investigating this question is also a future task.

6.3.2 Creep models

Both the Magic Formula and the brush tire model are widely used in the literature. However, we can choose a family of analytical functions that capture the essential properties of tire forces and are easier to be constructed. In the literature of contact mechanics and dynamics of railway wheelsets, this family of analytical functions are called *creep models*. See [27,30] for a detailed overview and [3] for an application example.

For creep models, the creep forces (i.e., the lateral tire forces in our model) can be characterized as functions of the *creep velocities*. Creep velocities are the theoretical velocities of the contact points within the scope of the rigid body model. In this study, the essential velocities are $v_{\mathrm{R}'}^{\mathrm{lat}}$ and $v_{\mathrm{L}'}^{\mathrm{lat}}$, which can be calculated by rearranging Eqs. (28)-(29) as

$$v_{\mathrm{R}'}^{\mathrm{lat}} = v_{\mathrm{R}'}^{\mathrm{long}} \tan\alpha_{\mathrm{R}} \,, \tag{87}$$

$$v_{\mathrm{L}'}^{\mathrm{lat}} = v_{\mathrm{L}'}^{\mathrm{long}} \tan\alpha_{\mathrm{L}} \,, \tag{88}$$

respectively.

Typical nonlinear creep models consist of two regions. For small creep velocities, the relation between the creep force and the creep velocity is linear. For large creep velocities, the creep force saturates at a certain value and the curve tends to the Coulomb-friction model. These regions can be combined with a sigmoid function [3,4]. For our analysis, the normalized tire force characteristics are calculated as

$$\mu(v^{\mathrm{lat}}) = \mu\,\mathrm{sigmoid}\left(\frac{\overline{c}_{\mathrm{lat}} v^{\mathrm{lat}}}{\mu N_0 v}\right) , \tag{89}$$

for both the right and the left wheels by substituting $\mu(v_{\mathrm{R}'}^{\mathrm{lat}})$ and $\mu(v_{\mathrm{L}'}^{\mathrm{lat}})$ in the formula. Using the relationships of Eqs. (87)-(88), one gets the normalized tire force characteristics given by the creep models as

$$\mu(\alpha) = \mu\,\mathrm{sigmoid}\left(\frac{\overline{c}_{\mathrm{lat}} \tan\alpha}{\mu N_0}\right) , \tag{90}$$

where the lateral creep coefficient $\overline{c}_{\mathrm{lat}}$ is assumed to be independent of the normal load. It is the slope of the characteristics at the origin, therefore it is equal to the normalized cornering stiffness $\overline{C}$ in the brush tire model, and the product BCD in the Magic Formula.

The sigmoid function in Eq. (90) denotes a class of functions with a unit slope at the origin, and tending to ± 1 at infinity. Some typical analytic sigmoid functions are the error function, the hyperbolic tangent function and an algebraic function with a square root:

$$\mathrm{sigmoid}(x) = \mathrm{erf}\left(\frac{\sqrt{\pi}}{2}x\right) , \tag{91}$$

$$\mathrm{sigmoid}(x) = \tanh(x) \,, \tag{92}$$

$$\mathrm{sigmoid}(x) = \frac{x}{\sqrt{1+x^2}} \,. \tag{93}$$

As a first step of the investigations, these three sigmoid functions are implemented in our model.

The normalized tire force characteristics calculated with the Magic Formula and the creep models are shown in Fig. 15. On the one hand, using sigmoid functions results in characteristics that have no peak, see Fig. 15(a). On the other hand, their smooth characteristics better match the characteristics of the Magic Formula for small side slip angles, see Fig. 15(b).

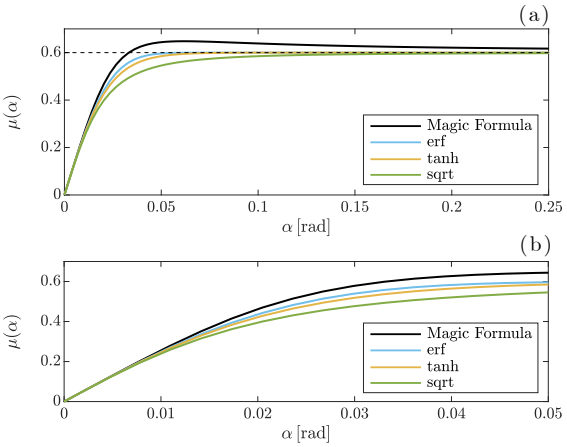


Fig. 15: The normalized tire force characteristics $\mu(\alpha)$ calculated with the Magic Formula and the creep models

The effect of using different creep models is shown in the bifurcation diagrams of Fig. 16 for both the uncontrolled and controlled trailers. In the case of the Magic Formula and the creep models, the unstable and stable periodic solutions are shown with black, light blue, yellow, and light green curves, respectively. When the Magic Formula and creep models are used, the normalized tire force characteristics are all smooth. Therefore, all unstable limit cycles emerge in a paraboloid structure, as also suggested in [7].

In addition, the characteristics of the bifurcation curves are very similar to those obtained with the Magic Formula. Implementing the error function (the function with the square root) in the model yields the closest (the farthest) match to the Magic Formula in the normalized tire force characteristics. Accordingly, the

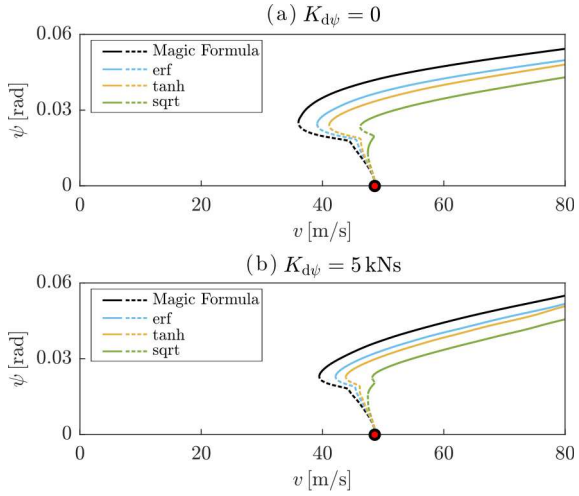


Fig. 16: Bifurcation diagrams for the yaw angle ψ with respect to the towing speed v with the Magic Formula and the creep models, (a) for $K_{d\psi} = 0$ and (b) for $K_{d\psi} = 5\,\mathrm{kNs}$

bifurcation curve is the one that most closely (least closely) resembles the one obtained with the Magic Formula.

Figure 16 shows that the used contact force model significantly affects nonlinear vibrations. Moreover, having a peak in the normalized tire force characteristics may not be very relevant. Simple functions can also adequately describe lateral tire forces.

7 Conclusions

A linear stability analysis with semi-discretization and a numerical bifurcation analysis with DDE-BIFTOOL were performed on a 4 DoF spatial mechanical model of two-wheeled trailers. The nonlinear governing equations of the system were summarized and precise calculations were carried out for the normal loads at the right and the left wheels, yielding an improved trailer model. A linear state feedback controller that incorporates a feedback delay and a dead zone was designed.

The nonlinear equations of motion were linearized around the steady-state and the linearized governing equations were summarized for the uncontrolled and controlled trailers. Linear stability charts showed the effects of the vertical position of the center of gravity and the applied control gain on linear stability. It was shown on bifurcation diagrams that the unsafe (bistable) zone can be reduced through differential braking of the wheels. Therefore, the globally stable towing speed region can be extended.

It was also demonstrated, that having a non-zero feedback delay can have a beneficial effect both on the linear and both on the nonlinear stability properties. Finally, our results showed that the contact force model used has a significant effect. Implementing the brush tire model and simple analytic functions (creep models) can affect the structure and the nature of the emerging limit cycles, and the vibration amplitudes. Creep models, formulated with simple functions, can adequately describe lateral tire forces.

Funding

The research reported in this paper was supported by the National Research, Development and Innovation Office under grant no. NKFI-150659 and NKFI-146201.

Conflict of interest

The authors declare that they have no conflict of interest.

References

1. Abdallah, C.T., Niculescu, S.I., Gu, K.: Some remarks on the delay stabilizing effect in siso systems. In: Proceedings of the 2003 American Control Conference (2003). DOI 10.1109/ACC.2003.1243481
2. Anderson, R.J., Kurtz, J.: Handling - characteristics simulations of car-trailer systems. SAE Transactions **89**, 2097–2113 (1980). URL http://www.jstor.org/stable/44633824
3. Antali, M.: Dynamics of railway wheelsets with a nonsmooth contact force model. In: J. Awrejcewicz (ed.) Perspectives in Dynamical Systems II — Numerical and Analytical Approaches, pp. 41–53. Springer International Publishing, Cham (2024)
4. Antali, M., Stepan, G.: On the nonsmooth dynamics of towed wheels. Meccanica **55**(12), 2523–2540 (2020). DOI 10.1007/s11012-020-01232-z
5. Balogh, T., Insperger, T.: Extending the admissible control-loop delays for the inverted pendulum by fractional-order proportional-derivative controller. Journal of Vibration and Control **30**(11-12), 2596–2604 (2024). DOI 10.1177/10775463231181662
6. Balogh, T., Kovacs, B.A., Insperger, T.: Human performance in virtual stabilization of a fractional-order system with reaction delay. J. R. Soc. Interface **21**(215) (2024). DOI https://doi.org/10.1098/rsif.2023.0685
7. Beregi, S.: Delay effects and non-smoothness in the dynamic tyre-road contact and vehicle steering. Phd thesis, Budapest University of Technology and Economics (2019)
8. Beregi, S., Avedisov, S.S., He, C.R., Takacs, D., Orosz, G.: Connectivity-based delay-tolerant control of automated vehicles: Theory and experiments. IEEE Transactions on Intelligent Vehicles **8**(1), 275–289 (2023). DOI 10.1109/TIV.2021.3131957
9. Beregi, S., Takacs, D., Gyebroszki, G., Stepan, G.: Theoretical and experimental study on the nonlinear dynamics of wheel-shimmy. Nonlinear Dynamics **98**, 2581–2593 (2019). DOI 10.1007/s11071-019-05225-w

10. Beregi, S., Takacs, D., Stepan, G.: Tyre induced vibrations of the car–trailer system. Journal of Sound and Vibration **362**, 214–227 (2016). DOI 10.1016/j.jsv.2015.09.015
11. Beregi, S., Takacs, D., Stepan, G.: Bifurcation analysis of wheel shimmy with non-smooth effects and time delay in the tyre–ground contact. Nonlinear Dynamics **98**, 841–858 (2019). DOI 10.1007/s11071-019-05123-1
12. Bernardis, M.D., Rini, G., Bottiglione, F., Hartavi, A.E., Sorniotti, A.: On nonlinear model predictive direct yaw moment control for trailer sway mitigation. Vehicle System Dynamics **61**(2), 445–471 (2023). DOI 10.1080/00423114.2022.2054352
13. Bevan, B.G., Smith, N.P., Ashley, C.: Some factors influencing the stability of car-caravan combinations. Proceedings of the IMechE Conferencein Road Vehicle Handling pp. 221–228 (1983). URL https://api.semanticscholar.org/CorpusID:107514096
14. Darling, J., Tilley, D., Gao, B.: An experimental investigation of car–trailer high-speed stability. Proceedings of the Institution of Mechanical Engineers, Part D: Journal of Automobile Engineering **223**(4), 471–484 (2009). DOI 10.1243/09544070jauto981
15. Davies, B.: Integral Transforms and their Applications, 3 edn. Springer (2002)
16. Edelmann, J., Haudum, M., Plöchl, M.: Bicycle rider control modelling for path tracking. IFAC-PapersOnLine **48**(1), 55–60 (2015). DOI 10.1016/j.ifacol.2015.05.070
17. Engelborghs, K., Luzyanina, T., Samaey, G.: DDE-BIFTOOL v. 2.00: a Matlab package for bifurcation analysis of delay differential equations. Department of Computer Science, K.U.Leuven (2001)
18. Facchini, G., Sekimoto, K., Courrech du Pont, S.: The rolling suitcase instability: a coupling between translation and rotation. Proceedings of the Royal Society A, Mathematical Physical and Engineering Sciences **473**, 1–28 (2017). DOI 10.1098/rspa.2017.0076
19. Gantmacher, F.: Lectures in analytical mechanics. MIR Publishers, Moscow (1975)
20. Hac, A., Fulk, D., Chen, H.: Stability and control considerations of vehicle-trailer combination. SAE Int. J. Passeng. Cars - Mech. Syst. **1**(1), 925–937 (2009). DOI 10.4271/2008-01-1228
21. Horvath, H.Z.: Stabilization of two-wheeled vehicles: trailers and electric scooters. Phd thesis, Budapest University of Technology and Economics (2025)
22. Horvath, H.Z., Feher, A.B., Takacs, D.: Nonlinear dynamics of a controlled two-wheeled trailer. In: G. Mastinu, F. Braghin, F. Cheli, M. Corno, S.M. Savaresi (eds.) 16th International Symposium on Advanced Vehicle Control, pp. 123–129. Springer Nature Switzerland, Cham (2024)
23. Horvath, H.Z., Takacs, D.: Modelling and simulation of rocking suitcases. In: Acta Polytechnica CTU Proceedings, vol. 18, p. 61–65 (2018). DOI 10.14311/APP.2018.18.0061
24. Horvath, H.Z., Takacs, D.: Stability and local bifurcation analyses of two-wheeled trailers considering the nonlinear coupling between lateral and vertical motions. Nonlinear Dynamics **107**(3), 2115–2132 (2022). DOI 10.1007/s11071-021-07120-9
25. Horvath, H.Z., Takacs, D.: Numerical analysis on shimmying wheels with dry friction damper. Periodica Polytechnica Mechanical Engineering **67**(2), 118–126 (2023). DOI 10.3311/PPme.21072
26. Insperger, T., Stepan, G.: Semi-Discretization for Time-Delay Systems. Springer New York (2011)
27. Johnson, K.L.: Contact Mechanics. Cambridge University Press (1985). DOI 10.1017/CBO9781139171731
28. Kadar, F., Stepan, G., Habib, G.: Model-free fold bifurcation prediction from pre-bifurcation scenario: experimental validation through wheel shimmy vibrations. Nonlinear Dynamics **113**(10), 11247–11258 (2025). DOI 10.1007/s11071-024-10686-9
29. Kageyama, I., Nagai, R.: Stabilization of passenger car-caravan combination using four wheel steering control. Vehicle System Dynamics **24**(4-5), 313–327 (1995). DOI 10.1080/00423119508969094
30. Kalker, J.J.: Three-Dimensional Elastic Bodies in Rolling Contact. Springer Dordrecht (1990). DOI 10.1007/978-94-015-7889-9
31. Kang, X., Deng, W.: Parametric study on vehicle–trailer dynamics for stability control. SAE Technical Paper Series (2003). DOI 10.4271/2003-01-1321
32. Kang, X., Deng, W.: Vehicle-trailer handling dynamics and stability control - an engineering review. SAE Technical Paper Series (2007). DOI 10.4271/2007-01-0822
33. Klinger, F., Nusime, J., Edelmann, J., Plöchl, M.: Wobble of a racing bicycle with a rider hands on and hands off the handlebar. Vehicle System Dynamics **52**, 51–68 (2014). DOI 10.1080/00423114.2013.877592
34. Kooijman, J.D.G., Schwab, A.L., Meijaard, J.P.: Experimental validation of a model of an uncontrolled bicycle. Multibody System Dynamics **19**, 115–132 (2008). DOI 10.1007/s11044-007-9050-x
35. Li, J., Takacs, D., Lu, J., Voros, I., Stepan, G.: Exploring optimal feedback delays of lane-keeping controller. Vehicle System Dynamics pp. 1–20 (2025). DOI 10.1080/00423114.2025.2532179
36. Lu, H., Habib, G., Wu, X., Ren, Y., Yan, L.: Application of nonlinear energy sink in suppressing wheel shimmy for advanced vehicle chassis design under independent wheel subsystems. Nonlinear Dynamics **112**(17), 14907–14923 (2024). DOI 10.1007/s11071-024-09726-1
37. Meijaard, J.P., Papadopoulos, J.M., Ruina, A., Schwab, A.L.: Linearized dynamics equations for the balance and steer of a bicycle: a benchmark and review. Proceedings of the Royal Society A **463**, 1955–1982 (2007). DOI 10.1098/rspa.2007.1857
38. Moreland, W.J.: The story of shimmy. Journal of the Aeronautical Sciences **21**(12), 793–808 (1954). DOI 10.2514/8.3227
39. Pacejka, H.: Tyre and Vehicle Dynamics. Elsevier Butterworth-Heinemann (2002)
40. Pacejka, H.B.: The wheel shimmy phenomenon. Phd thesis, Technical University of Delft (1966)
41. Plöchl, M., Edelmann, J., Angrosch, B., Ott, C.: On the wobble mode of a bicycle. Vehicle System Dynamics **50**(3), 415–429 (2012). DOI 10.1080/00423114.2011.594164
42. Ren, Y., Lu, H., Habib, G., Shi, L., Zhang, N., Wu, X.: Wheel shimmy suppression through the piecewise nonlinear energy sink: elimination of detrimental isolas. Nonlinear Dynamics **113**(18), 24225–24244 (2025). DOI 10.1007/s11071-025-11389-5
43. Schlippe, B., Dietrich, R.: Das Flattern Eines Bepneuten Rades (Shimmying of a pneumatic wheel). In: Bericht 140 der Lilienthal-Gesellschaft für Luftfahrtforschung, pp. 35–45, 63–66 (1941). English translation is available in *NACA Technical Memorandum* 1365, pp. 125-166, 217-228, 1954
44. Schwab, A.L., Meijaard, J.P., Papadopoulos, J.M.: Benchmark results on the linearized equations of motion of an uncontrolled bicycle. Journal of Mechanical

Science and Technology **19**(S1), 292–304 (2005). DOI 10.1007/bf02916147
45. Sharp, R.S., Evangelou, S., Limebeer, D.J.N.: Advances in the modelling of motorcycle dynamics. Multibody System Dynamics **12**(3), 251–283 (2004). DOI 10.1023/B:MUBO.0000049195.60868.a2
46. Sharp, R.S., Fernańdez, M.A.A.: Car-caravan snaking - part 1: the influence of pintle pin friction. In: Proceedings of the Institution of Mechanical Engineers Part C - Journal of Mechanical Engineering Science, 7, vol. 216, pp. 707–722 (2002). DOI 10.1243/09544060260128760
47. Stepan, G.: Delay, nonlinear oscillations and shimmying wheels pp. 373–386 (1999). DOI 10.1007/978-94-011-5320-1_38
48. Szaksz, B., Stepan, G.: Delay-induced bifurcations in collocated position control of an elastic arm. Nonlinear Dynamics **107**, 1611–1622 (2022). DOI 10.1007/s11071-021-06812-6
49. Szaksz, B., Stepan, G.: Delay effects in the dynamics of human controlled towing of vehicles. Journal of Computational and Nonlinear Dynamics **18**(6) (2023). DOI 10.1115/1.4056590
50. Takacs, D., Orosz, G., Stepan, G.: Delay effects in shimmy dynamics of wheels with stretched string-like tyres. European Journal of Mechanics - A/Solids **28**(3), 516–525 (2009). DOI https://doi.org/10.1016/j.euromechsol.2008.11.007
51. Troger, H., Zeman, K.: A nonlinear-analysis of the generic types of loss of stability of the steady-state motion of a tractor-semitrailer. Vehicle System Dynamics **13**(4), 161–172 (1984). DOI 10.1080/00423118408968773
52. Vempaty, S., He, Y., Zhao, L.: An overview of control schemes for improving the lateral stability of car-trailer combinations. International Journal of Vehicle Performance **6**(2), 151–199 (2020). DOI 10.1504/IJVP.2020.106985
53. Whitcomb, D.W., Milliken, W.F.: Design implications of a general theory of automobile stability and control. Proceedings of the Institution of Mechanical Engineers: Automobile Division **10**(1), 367–425 (1956). DOI 10.1243/pime_auto_1956_000_035_02